

THz Near-Field Imaging of Extreme Subwavelength Metal Structures

Xinzhong Chen,[†] Xiao Liu,[†] Xiangdong Guo, Shu Chen, Hai Hu, Elizaveta Nikulina, Xinlin Ye, Ziheng Yao, Hans A. Bechtel, Michael C. Martin, G. Lawrence Carr, Qing Dai,^{*} Songlin Zhuang, Qing Hu, Yiming Zhu,^{*} Rainer Hillenbrand, Mengkun Liu,^{*} and Guanjun You^{*}Cite This: *ACS Photonics* 2020, 7, 687–694

Read Online

ACCESS |



Metrics & More



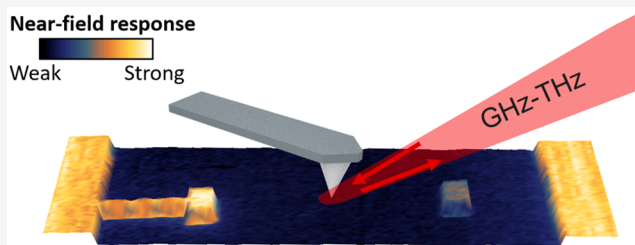
Article Recommendations



Supporting Information

ABSTRACT: Modern scattering-type scanning near-field optical microscopy (s-SNOM) has become an indispensable tool in material research. However, as the s-SNOM technique marches into the far-infrared (IR) and terahertz (THz) regimes, emerging experiments sometimes produce puzzling results. For example, “anomalies” in the near-field optical contrast have been widely reported. In this Letter, we systematically investigate a series of extreme subwavelength metallic nanostructures via s-SNOM near-field imaging in the GHz to THz frequency range. We find that the near-field material contrast is greatly impacted by the lateral size of the nanostructure, while the spatial resolution is practically independent of it. The contrast is also strongly affected by the connectivity of the metallic structures to a larger metallic “ground plane”. The observed effect can be largely explained by a quasi-electrostatic analysis. We also compare the THz s-SNOM results to those of the mid-IR regime, where the size-dependence becomes significant only for smaller structures. Our results reveal that the quantitative analysis of the near-field optical material contrasts in the long-wavelength regime requires a careful assessment of the size and configuration of metallic (optically conductive) structures.

KEYWORDS: scattering-type scanning near-field optical microscopy (s-SNOM), near-field, THz, nanoimaging, Schottky diodes



The best spatial resolution that can possibly be achieved with a conventional optical microscope is fundamentally constrained by the diffraction limit to roughly half of the incident wavelength, prohibiting nanoscale optical characterization.¹ In an effort to overcome this limit, the scattering-type scanning near-field optical microscope (s-SNOM) was developed. The tip-scattered light conveys local sample information and is detected by a conventional far-field detector. In this case, the spatial resolution is determined predominantly by the tip apex radius, tapping amplitude, and demodulation order, and as such is essentially independent of the incident wavelength.² Since its introduction, s-SNOM nanoimaging and spectroscopy have aided numerous scientific advances such as direct spatial mapping of surface polaritons, spatial phase coexistence, and electromagnetic field localization.^{3–11}

The spectral region spanning 0.1–10 terahertz (THz) is commonly recognized as the “THz gap” because of technical difficulties in the generation and detection of intense coherent THz light.¹² Performing s-SNOM at THz frequencies poses even greater challenges: conventional AFM probes are extreme subwavelength objects, resulting in low coupling and scattering efficiency. Nevertheless, intense research efforts by the THz s-SNOM community have led to significant technical and instrumental advances in recent years,^{13–26} enabling nanoimaging in the 50 GHz to 5 THz spectral region for accessing local conductivity and phase coexistence.

The deep-subwavelength scale spatial resolution achievable via s-SNOM can be largely attributed to the tight electromagnetic field confinement below the tip apex.^{27,28} This fact sometimes leads to the misconception that the near-field optical contrast is solely governed by the optical properties, i.e. dielectric constants or optical conductivity, of the sample volume right under the tip apex. However, recent THz s-SNOM experiments provide some contradicting and counterintuitive yet fundamentally interesting observations. For example, it has been reported that isolated metallic structures exhibit a lower near-field contrast compared to large and connected ones, even though the spatial resolution of THz s-SNOM is much higher than the structure size.²² It has also been reported that AFM tips with larger apex radii increase the THz near-field amplitude and contrast, while leaving the spatial resolution nearly unaffected.²⁸ In this Letter, we describe systematic THz and mid-IR near-field imaging of a series of metallic nanostructures. These findings suggest that in addition to intrinsic material properties, the size and configuration of

Received: October 21, 2019

Published: January 29, 2020



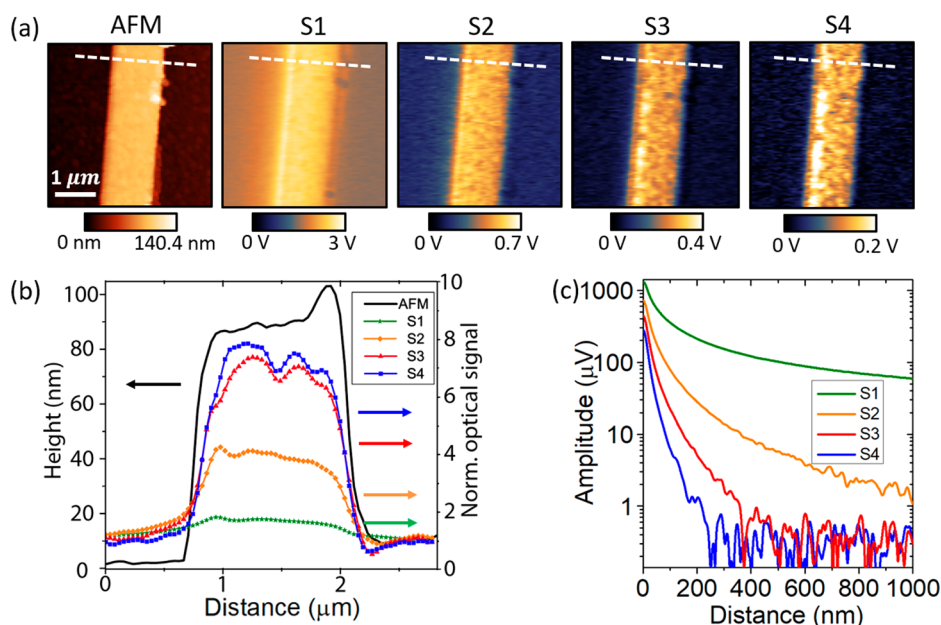


Figure 1. Assessment of spatial resolution and signal-to-noise ratio obtained via THz *s*-SNOM. (a) Left to right: AFM topographic image and near-field images demodulated at different harmonics of the tip's tapping frequency. (b) Height and near-field optical signal profiles along the white dashed lines in (a). S1 through S4 are normalized to the average substrate signal in their corresponding images to yield a relative contrast. (c) Approach curves for different orders of demodulation on gold bar.

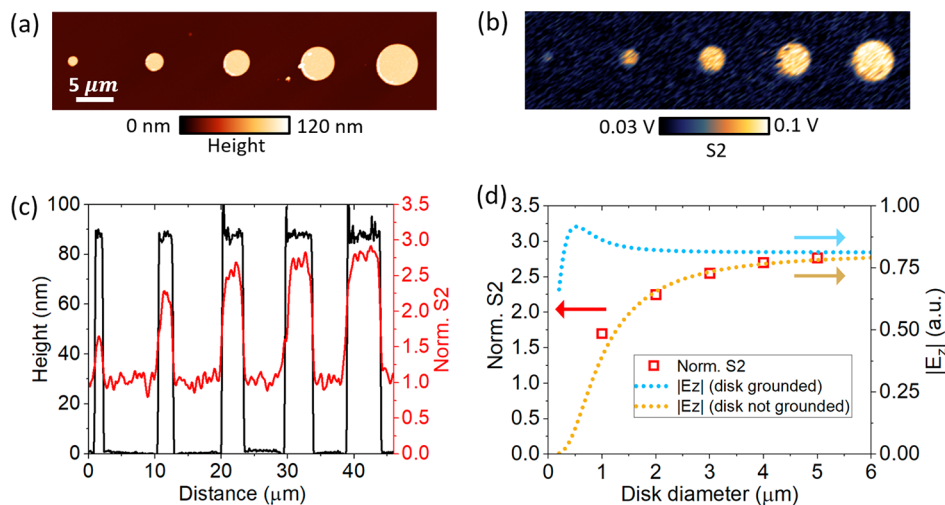


Figure 2. (a) AFM image of a series of micron-sized gold disks. (b) The corresponding second harmonic near-field amplitude image at 171.84 GHz (1.74 mm), which shows an increasing near-field response with increasing disk diameter. (c) Height and normalized near-field S2 optical signal profiles across the disks in (a) and (b). The height of the disk is constant (~ 80 nm), while S2 increases with increasing disk diameter. (d) Red squares: average and normalized near-field signal (S2) of the disks with different diameters. Brown and blue curves represent the calculated electric field at the point charge for ungrounded and grounded disks, respectively.

the probed nanostructure in the deep subwavelength regime plays important roles for near-field optical material contrasts.

We first use a home-built *s*-SNOM setup to perform sub-THz near-field imaging. The system utilizes high-harmonic (12th) generation from a microwave source.^{15,25} A signal generator produces a microwave signal (9–14.6 GHz), which is then frequency multiplied through Schottky diodes. This generates a coherent sub-THz wave (110–175 GHz), which is directly focused onto the tip of an atomic force microscope (AFM; Bruker Multimode). The AFM is operating at tapping mode with frequency Ω . The second signal generator supplies microwave radiation at a slightly different frequency to another Schottky diode, which functions as both the detector and the

reference light generator. The frequency difference between the incident light and the reference light is set to be $\Delta\Omega = 24$ MHz. The second Schottky diode is connected to a Lock-in amplifier (Zurich HF2LI), which demodulates the signal at $n\Omega - m\Delta\Omega$ as a mean of phase-resolved imaging and far-field background suppression.²⁹ To improve the light coupling efficiency between the THz wave and the AFM tip,^{27,28} we use customized tips (Rocky Mountain Nanotechnology, LLC) of length about 200 μm and apex radius about 100 nm. The tips are longer and have a larger apex radius compared to typical AFM tips used for IR or visible *s*-SNOM, thus, greatly enhancing the THz scattering and improving the signal-to-noise ratio.²⁸ All of our THz *s*-SNOM experiments use a

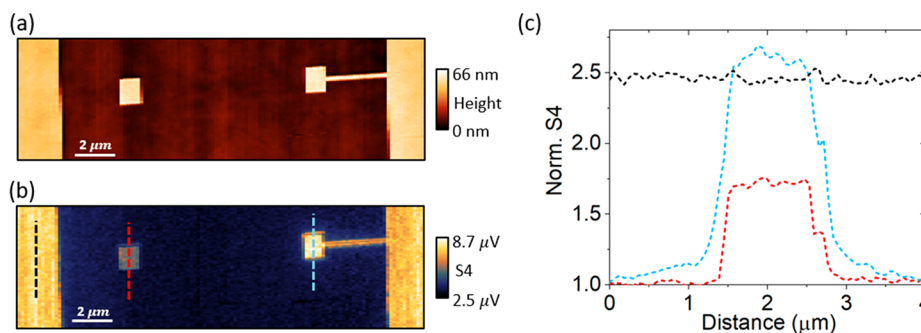


Figure 3. (a) AFM topography image of an isolated gold square patch and a connected gold square patch. (b) The corresponding fourth harmonic near-field image (S4) at 2.52 THz (119 μm). (c) Normalized near-field S4 profiles along the indicated dashed lines in (b). The black curve is across the large gold pad. The blue curve is across the connected gold patch. The red curve is across the isolated gold patch.

typical tapping frequency of $\Omega \sim 40$ kHz with a tapping amplitude around 100 nm.

We first characterize the spatial resolution of our THz s-SNOM setup via imaging a ~ 90 nm thick by ~ 1.5 μm wide gold bar antenna on a SiO_2 substrate. AFM topography and near-field amplitude images demodulated at the first (S1), second (S2), third (S3), and fourth (S4) harmonic orders are shown in Figure 1a. A clear material contrast between gold and SiO_2 is observed in all of the demodulated near-field amplitude images. Height and near-field optical signal profiles across the bar (designated by the white dashed lines) are displayed in Figure 1b. The near-field amplitude signals are normalized to the averaged substrate signal. The near-field optical resolution is similar to the AFM resolution and is mainly limited by the AFM tip apex radius. When a topographic boundary is present, it is difficult to precisely evaluate the optical resolution due to the unknown slope of the edge and edge-darkening artifact.³⁰ However, based on the edge profile of the optical signal, we conservatively estimate that the resolutions for AFM and S2 to be 120 and 200 nm based on 90 to 10% signal width, similar to previously reported spatial resolution of THz s-SNOM and other microwave scanning probe techniques.^{31,32} Nonetheless, we achieved a near-field resolution in the order of $\lambda/10^4$ with second harmonic demodulation at ~ 100 GHz range. Note that the relative contrast in the S1 image is rather weak due to an undesirable far-field background signal, which is confirmed by the approach curves in Figure 1c, wherein the S1 approach curve does not significantly subside even at a tip–sample distance of 1 μm , while the S2–S4 curves quickly decay. Similar to typical IR s-SNOMs, demodulation up to at least the second harmonic order is necessary in order to effectively suppress the background. Furthermore, statistical analysis of the signal variation on gold indicates that the S2 signal-to-noise ratio is at least 10:1. The optical signals appear to be slightly higher on the left side of the gold bar. We attribute this to a scanning induced artifact due to the uneven surface of the sample.

Next we demonstrate that the near-field material contrast of s-SNOM depends strongly on the size of the metallic structures, although the spatial resolution is nearly independent of the structure size. We first study gold disks of diameters from 1 to 5 μm , fabricated on a SiO_2 substrate (AFM image shown in Figure 2a). From common knowledge one could assume an identical near-field material contrast for all disks, except for cases in which antenna effects or polaritonic responses occur (which is not the case here, as disks are of deep subwavelength scale). However, the THz s-SNOM

amplitude images show a clear decrease of the near-field amplitude signal of the disk with decreasing disk diameter (Figure 2b). Line profiles across the disk centers (Figure 2c) show the effect more clearly. Note that even the smallest disk size (1 μm diameter) is much larger than the spatial resolution. Only the S2 images are displayed without loss of generality because the S3 and S4 images show the same trend. A qualitatively similar phenomenology has been experimentally observed with scanning probe technique combined with difference-frequency generation where the frequency difference between two incident CO_2 lasers (both at ~ 10 μm wavelength) is set to 9 GHz.^{33,34} The authors observed difference-frequency generation signal from the metallic disks with different sizes. They postulated that the disk-size-dependent difference-frequency generation signal is related to the periodic charge distributions on the tip and the disks induced by the incident radiations at ~ 10 μm wavelength. This is not applicable in our case because the incident wavelength used in our experiments is orders of magnitude larger than the length of the tip shank and the disk diameter such that the spatially periodic charge distribution is unlikely to form.

Inspired by previous works on electrostatic force microscopy,^{35,36} we propose an electrostatic “toy-model” for our experimental data. The electrostatic limit is justified due to the much longer incident wavelength compared to the size of the tip and the nanostructures. For simplicity, we model the tip by an electrical monopole with charge q located near the tip apex. Then the electrostatic problem of a point charge above a conducting disk can be solved analytically with a clean solution.^{37,38} Suppose the point charge is located at $(0, 0, z_0)$ above the center of a grounded metal disk of radius a in the x – y plane, the potential on the z axis due to both the point charge and the induced surface charge on the disk is given by³⁸

$$V_1(z) = \frac{2q}{\pi(z^2 - z_0^2)} \left[z_0 \tan^{-1}\left(\frac{a}{z}\right) - z \tan^{-1}\left(\frac{a}{z_0}\right) \right] \quad (1)$$

If the disk is not grounded, its potential picks up an extra term due to the presence of balancing charges with opposite sign (to make sure the disk is charge neutral) and becomes

$$V_2(z) = V_1(z) + \frac{2q}{a\pi} \tan^{-1}\left(\frac{a}{z}\right) \tan^{-1}\left(\frac{a}{z_0}\right) \quad (2)$$

In Figure 2d, we calculate the trend of the electric field at the position right below the monopole $|E_z(z_0 \approx 250 \text{ nm})| = \left| -\frac{dV(z)}{dz} \right|_{z=z_0}$ as a function of disk

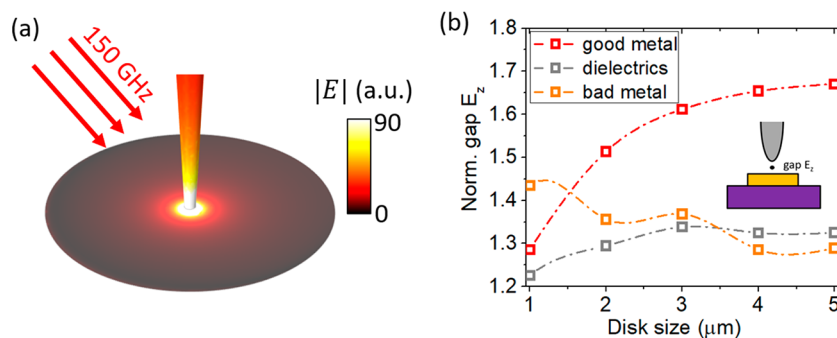


Figure 4. (a) Simulation geometry and typical electric field distribution. (b) Normalized electric field in the tip-sample gap as a function of disk diameter for three categories of material: a good metal ($\epsilon_1 \rightarrow -\infty$, $\epsilon_2 \rightarrow \infty$), a dielectric material ($\epsilon_1 = 10$, $\epsilon_2 = 0.1$), and a bad metal ($\epsilon_1 = -10$, $\epsilon_2 = 10$).

diameter d for both grounded (blue curve) and ungrounded (brown curve) scenarios. The balancing charge in the case of ungrounded disks is found to be of significant importance for the change of the electric field, which is consistent with the size dependent trend of the averaged S2 signal of the disks (red squares in Figure 2d). On the other hand, when the disk is grounded, the electric field is predicted to be constant at $d > 1 \mu\text{m}$, as we demonstrate below.

In an earlier THz nanoimaging work by Kuschewski et al., small and isolated gold islands have been observed to exhibit a lower near-field signal compared to large and connected islands.²² This was attributed phenomenologically to the weaker polarizability of the small isolated islands. Here using the electrostatic model, we can provide quantitative insights into this intriguing observation. As suggested by eq 1 and the blue curve in Figure 2d, if the condition of local charge neutrality is broken by connecting the small disks to the ground or a large gold pad (as a charge reservoir), the near-field signal will be significantly boosted. To test this effect, nanoimaging is performed on two identical gold square patches, with one isolated and the other connected to a large gold pad (Figure 3). Here we use a commercial s-SNOM (Neaspec GmbH, Germany) with a tunable THz gas laser (SIFIR-50, Coherent Inc., U.S.A.) operating at 2.52 THz. The scattered light is collected interferometrically in a homodyne scheme by a cryogen-free THz bolometer (QMC Instruments Ltd., Cardiff, U.K.). Simultaneously obtained AFM topography and fourth harmonic near-field amplitude image are shown in Figure 3a,b. Corresponding line profiles across the gold patches and large gold pad are shown in Figure 3c. Despite the fact that two gold patches have the same thickness $\sim 50 \text{ nm}$ and lateral size $\sim 1 \mu\text{m}$, the near-field responses are drastically different. The connected gold patch exhibits a significantly stronger near-field signal (S4) than the isolated one, even slightly stronger than the large gold pad. This observation is consistent with the expectation and supports the validity of our electrostatic analysis. This result can also be directly compared to the work by Kuschewski et al.²²

Overall, our phenomenological model yields a qualitative interpretation of the observed phenomenon. However, we postulate that the underlying physics can be much more complex. Besides the above-described effect, other effects may be responsible for the observed size-dependent near-field contrast which deserves further investigation. For example, beyond the electrostatic limit, surface inductance is found to be weakened in smaller metallic structures. The decreased inductance leads to a relatively more important contribution

from the disk resistance, which leads to a higher eddy current damping in the near-field. This may greatly reduce the electric field intensity thus the near-field scattering signal (this analysis will be reported by S. T. Chui elsewhere).

While a full analytical electrodynamic model remains challenging, full-wave simulations of the tip-disk-substrate system are more probable and can be carried out using the finite element method (COMSOL). The scale mismatch among incident wavelength (1.74 mm), tip length (200 μm), and tip-sample distance (0–100 nm) makes a rigorous simulation of the near-field signal computationally expensive.^{28,30,39–41} Instead, we use the electric field enhancement factor (electric field normalized to incident field) inside the tip-sample gap as an indirect gauge for the near-field interaction, a well-established approach within the community. It was recently demonstrated that the local field enhancement does not necessarily reflect the scattering intensity when the tip radii are different.²⁸ For example, enlarging a tip radius results in weaker local field enhancement even though it also makes the scattering intensity much higher. However, for a constant tip radius, the field enhancement and detected near-field signal are expected to be positively correlated.²⁷ Here we simulate the total electric field enhancement under the tip volume by modeling the tip as a cone of 200 μm shank length and 100 nm radius at its bottom, which resembles realistic tip geometry. The disk on the SiO_2 substrate is set to be 100 nm beneath the tip apex. An incident plane wave of 150 GHz frequency approaches the sample at a 60° angle with respect to the surface normal.

The simulation layout and typical electric field distribution are shown in Figure 4a. The field inside the gap between the tip and the disk is closely monitored as the disk size increases from 1 to 5 μm . To extend the generality of the simulation, we test three categories of material by adjusting the disk permittivity $\epsilon = \epsilon_1 + i\epsilon_2$ for a good metal ($\epsilon_1 \rightarrow -\infty$, $\epsilon_2 \rightarrow \infty$), a dielectric material ($\epsilon_1 = 10$, $\epsilon_2 = 0.1$), and a bad metal ($\epsilon_1 = -10$, $\epsilon_2 = 10$). Field enhancement normalized to that of a “vacuum disk” ($\epsilon_1 = 1$, $\epsilon_2 = 0$) as a function of disk diameter is shown in Figure 4b. Of the three materials, only the good metal exhibits a significant, monotonically increasing field enhancement, as is consistent with our experimental observations. The field enhancements of the dielectric materials and bad metals are noticeably less affected by increasing disk diameter due to the lack of mobile charge carriers.

From the simulations, we conclude that the aforementioned size-dependent, near-field contrast is most prominent in good

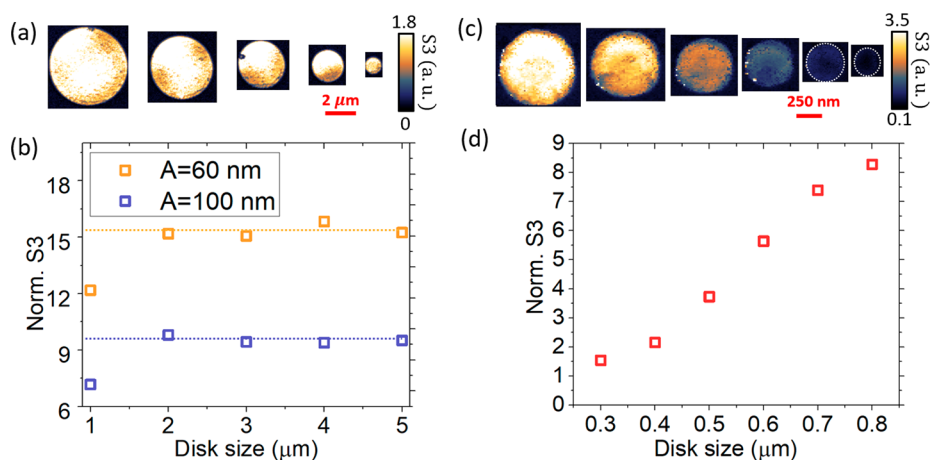


Figure 5. (a) Near-field (S3) images on disks of diameter 1, 2, 3, 4, and 5 μm . (b) Average S3 contrast as a function of disk diameter. The dashed lines indicate the saturation signal level. A is the tip tapping amplitude. (c) Near-field (S3) images of disks of diameter 300, 400, 500, 600, 700, and 800 nm. White circles indicate the boundaries of the disks. (d) Average S3 contrast as a function of disk diameter. The dashed line indicates a linear trend.

metals, which have significant surface charge or current. The THz near-field signals of dielectrics or bad metals should not exhibit significant dependence for sample sizes at the micron scale ($\sim\lambda/100$). Unfortunately, the scale mismatch between the wavelength (~ 2 mm), tip length (~ 200 μm), disk diameter (~ 1 μm), and the tip apex radius (100 nm) currently prevents us from performing further systematic simulations to investigate the fine details of the tip–sample scattering process, such as the emission pattern, charge distribution, and dipole moment of the tip.^{28,41} These aspects remain to be studied when time and computation power allow in the future.

For comparison, we examine the size-dependent near-field material contrast in the mid-IR regime. Near-field imaging at ~ 6 μm wavelength is performed via a commercial s-SNOM (Neaspec GmbH, Germany) equipped with a quantum cascade laser (Daylight Solutions, U.S.A.). Figure 5a shows S3 amplitude images of the same gold disks previously studied. Compared to the THz near-field images, no significant size-dependence is observed in the optical response of the mid-IR images for disks larger than 1 μm . An average near-field contrast as a function of disk size is plotted in Figure 5b for two different tapping amplitudes. Increasing the tapping amplitude diminishes the overall contrast, but has no significant effect on the trend of the optical response versus disk size. Unlike the sub-THz near-field signal, that of mid-IR quickly saturates when the disk size exceeds 1 μm . We further investigate by studying smaller disks of diameter 300–800 nm, whose responses quickly decay with decreasing disk size, as shown in Figure 5c,d. The trend can still be phenomenologically fitted by the quasi-electrostatic analysis in eq 1 with a smaller charge-disk distance z_0 , but the much shorter wavelength of mid-IR radiation, in principle, makes the quasi-electrostatic assumption quantitatively invalid. A similar analysis with consideration of the retardation should be more appropriate, but it is beyond the scope of this work since a simple analytical form cannot be easily obtained, and not much more physical insight is gained from such a treatment.

To demonstrate that this phenomenon is not limited to a particular frequency, mid-IR broadband near-field spectroscopy is performed on the same disk samples. Indeed, a similar trend is observed in the whole frequency range between 400 and 1100 cm^{-1} (Supporting Information, S2). Furthermore,

we find that demodulation order also has a minimal impact on trend of the near-field contrast (Supporting Information, S3).

In the end, we would like to note that, in some of the gold disks, mid-IR nanoimaging reveals plasmonic patterns that are spatially inhomogeneous. This is because the sizes of these disks are comparable to the incident wavelength where the antenna effect is prominent.^{39,42–44} Similar antenna effect is absent in the THz nanoimages due to the scale mismatch. To our best knowledge so far, there is only one published report on THz near-field imaging of the antenna effects using s-SNOM.⁴⁵ Further investigations still await.

Without considering polaritonic or antenna effects, current understanding of s-SNOM suggests that the near-field material contrasts are determined by the local dielectric properties of the sample and data acquisition parameters (tip radius, tapping amplitude, demodulation order, etc.). Therefore, theoretical attempts to calculate the near-field contrast typically model the sample as a homogeneous semi-infinite half-space^{2,46–49} or layered planes,^{50,51} neglecting lateral inhomogeneity. These assumptions are largely valid for samples of bad metals or dielectric insulators.^{52,53} However, our study shows that in metallic structures smaller than $\sim 1/100$ λ in the THz region and $\sim 1/10$ λ in the IR region, the sample size can significantly affect the near-field contrast and demands further theoretical investigations. Together with previous reports^{54–56} demonstrating the IR near-field resonance effect in metallic structures of size $\sim 1/10$ λ to ~ 1 λ , this work suggests that geometric factors in metals are indeed important and need to be carefully addressed in the nanoimaging process with s-SNOM.⁴²

■ ASSOCIATED CONTENT

Supporting Information

The Supporting Information is available free of charge at <https://pubs.acs.org/doi/10.1021/acsphotonics.9b01534>.

S1: THz nanoimaging on linear antennas with different lengths; S2: Mid-IR broadband spectroscopy on gold disks; S3: Effect of demodulation order on near-field contrast (PDF)

AUTHOR INFORMATION**Corresponding Authors**

Qing Dai – Division of Nanophotonics, CAS Key Laboratory of Standardization and Measurement for Nanotechnology, CAS Center for Excellence in Nanoscience, National Center for Nanoscience and Technology, Beijing 100190, China; Email: daiq@nanoctr.cn

Yiming Zhu – Shanghai Key Lab of Modern Optical Systems, Terahertz Technology Innovation Research Institute, and Engineering Research Center of Optical Instrument and System, Ministry of Education, University of Shanghai for Science and Technology, Shanghai 200093, China; Email: ymzhu@usst.edu.cn

Mengkun Liu – Department of Physics and Astronomy, Stony Brook University, Stony Brook, New York 11794, United States; National Synchrotron Light Source II, Brookhaven National Laboratory, Upton, New York 11973, United States; Email: mengkun.liu@stonybrook.edu

Guanjun You – Shanghai Key Lab of Modern Optical Systems, Terahertz Technology Innovation Research Institute, and Engineering Research Center of Optical Instrument and System, Ministry of Education, University of Shanghai for Science and Technology, Shanghai 200093, China; Email: gjyou@usst.edu.cn

Authors

Xinzhong Chen – Department of Physics and Astronomy, Stony Brook University, Stony Brook, New York 11794, United States; orcid.org/0000-0002-6103-3848

Xiao Liu – Shanghai Key Lab of Modern Optical Systems, Terahertz Technology Innovation Research Institute, and Engineering Research Center of Optical Instrument and System, Ministry of Education, University of Shanghai for Science and Technology, Shanghai 200093, China

Xiangdong Guo – Division of Nanophotonics, CAS Key Laboratory of Standardization and Measurement for Nanotechnology, CAS Center for Excellence in Nanoscience, National Center for Nanoscience and Technology, Beijing 100190, China

Shu Chen – CIC nanoGUNE BRTA, 20018 Donostia-San Sebastián, Spain

Hai Hu – Division of Nanophotonics, CAS Key Laboratory of Standardization and Measurement for Nanotechnology, CAS Center for Excellence in Nanoscience, National Center for Nanoscience and Technology, Beijing 100190, China

Elizaveta Nikulina – CIC nanoGUNE BRTA, 20018 Donostia-San Sebastián, Spain

Xinlin Ye – Shanghai Key Lab of Modern Optical Systems, Terahertz Technology Innovation Research Institute, and Engineering Research Center of Optical Instrument and System, Ministry of Education, University of Shanghai for Science and Technology, Shanghai 200093, China

Ziheng Yao – Department of Physics and Astronomy, Stony Brook University, Stony Brook, New York 11794, United States; Advanced Light Source Division, Lawrence Berkeley National Laboratory, Berkeley, California 94720, United States

Hans A. Bechtel – Advanced Light Source Division, Lawrence Berkeley National Laboratory, Berkeley, California 94720, United States

Michael C. Martin – Advanced Light Source Division, Lawrence Berkeley National Laboratory, Berkeley, California 94720, United States

G. Lawrence Carr – National Synchrotron Light Source II, Brookhaven National Laboratory, Upton, New York 11973, United States

Songlin Zhuang – Shanghai Key Lab of Modern Optical Systems, Terahertz Technology Innovation Research Institute, and Engineering Research Center of Optical Instrument and System, Ministry of Education, University of Shanghai for Science and Technology, Shanghai 200093, China

Qing Hu – Department of Electrical Engineering and Computer Science and Research Laboratory of Electronics, Massachusetts Institute of Technology, Cambridge, Massachusetts 02139, United States

Rainer Hillenbrand – CIC nanoGUNE BRTA, 20018 Donostia-San Sebastián, Spain; Department of Electricity and Electronics, UPV/EHU, 20018 Donostia-San Sebastián, Spain; IKERBASQUE, Basque Foundation of Science, 48013 Bilbao, Spain; orcid.org/0000-0002-1904-4551

Complete contact information is available at:
<https://pubs.acs.org/10.1021/acsp Photonics.9b01534>

Author Contributions

[†]These authors contributed equally to this work.

Notes

The authors declare the following competing financial interest(s): R.H. is a co-founder of Neaspec GmbH, a company producing scattering-type scanning near-field optical microscope systems such as the one used in this study. The other authors declare no competing interests.

ACKNOWLEDGMENTS

G.Y. acknowledges support from the National Key Research and Development Program of China (Grant Nos. 2017YFF0106304 and 2016YFF0200306). Y. Z. acknowledges support from the National Natural Science Foundation of China (61722111), 111 Project (D18014), and International Joint Lab Program supported by Science and Technology Commission Shanghai Municipality (17590750300). CAS authors acknowledge the support from the National Natural Science Foundation of China (Grant Nos. 11674073, 11704085, 51925203, 51972074, 51902065). Stony Brook University authors acknowledge support from National Science Foundation under Grant No. DMR-1904576. Part of this work was also supported by the RISE2 node of NASA's Solar System Exploration Research Virtual Institute under NASA Cooperative Agreement 80NSSC19MO2015. The CIC nanoGUNE authors acknowledge support from the Spanish Ministry of Economy, Industry, and Competitiveness (National Project RTI2018-094830-B-100 and the Project MDM-2016-0618 of the Marie de Maeztu Units of Excellence Program), the Basque Government (Grant No. IT1164-19), and the H2020 FET OPEN Project PETER (GA#767227). G.Y. thanks the Young Eastern Scholar at Shanghai Institutions of Higher Learning. This research used resources of the Advanced Light Source, which is a DOE Office of Science User Facility under Contract No. DE-AC02-05CH11231. Z.Y. acknowledges the support from the ALS Doctoral Fellowship in Residence Program. The authors would like to thank Dr. Oleg Butyaev (NT-MDT), Prof. S. T. Chui (University of Delaware), Dr. Alexander Mcleod (Columbia University), and Prof. D. N. Basov (Columbia University) for the helpful discussions.

REFERENCES

- (1) Abbe, E. Beiträge Zur Theorie Des Mikroskops Und Der Mikroskopischen Wahrnehmung. *Arch. für Mikroskopische Anat.* **1873**, *9* (1), 413–418.
- (2) Hillenbrand, R.; Keilmann, F. Complex Optical Constants on a Subwavelength Scale. *Phys. Rev. Lett.* **2000**, *85* (14), 3029–3032.
- (3) Chen, X.; Hu, D.; Mescall, R.; You, G.; Basov, D. N.; Dai, Q.; Liu, M. Modern Scattering-Type Scanning Near-Field Optical Microscopy for Advanced Material Research. *Adv. Mater.* **2019**, *31* (24), 1804774.
- (4) Liu, M.; Sternbach, A. J.; Basov, D. N. Nanoscale Electrodynamics of Strongly Correlated Quantum Materials. *Rep. Prog. Phys.* **2017**, *80* (1), 014501.
- (5) Fei, Z.; Andreev, G. O.; Bao, W.; Zhang, L. M.; McLeod, A. S.; Wang, C.; Stewart, M. K.; Zhao, Z.; Dominguez, G.; Thieme, M.; et al. Infrared Nanoscopy of Dirac Plasmons at the Graphene-SiO₂ Interface. *Nano Lett.* **2011**, *11*, 4701–4705.
- (6) Dai, S.; Fei, Z.; Ma, Q.; Rodin, A. S.; Wagner, M.; McLeod, A. S.; Liu, M. K.; Gannett, W.; Regan, W.; Watanabe, K.; et al. Tunable Phonon Polaritons in Atomically Thin van Der Waals Crystals of Boron Nitride. *Science (Washington, DC, U. S.)* **2014**, *343* (6175), 1125–1129.
- (7) McLeod, A. S.; van Heumen, E.; Ramirez, J. G.; Wang, S.; Saerbeck, T.; Guenon, S.; Goldflam, M.; Andreev, L.; Kelly, P.; Mueller, A.; et al. Nanotextured Phase Coexistence in the Correlated Insulator V₂O₃. *Nat. Phys.* **2017**, *13* (1), 80–86.
- (8) Chen, J.; Badioli, M.; Alonso-González, P.; Thongrattanasiri, S.; Huth, F.; Osmond, J.; Spasenović, M.; Centeno, A.; Pesquera, A.; Godignon, P.; et al. Optical Nano-Imaging of Gate-Tunable Graphene Plasmons. *Nature* **2012**, *487* (7405), 77–81.
- (9) Rang, M.; Jones, A. C.; Zhou, F.; Li, Z.-Y.; Wiley, B. J.; Xia, Y.; Raschke, M. B. Optical Near-Field Mapping of Plasmonic Nanoprisms. *Nano Lett.* **2008**, *8* (10), 3357–3363.
- (10) Jiang, T.; Kravtsov, V.; Tokman, M.; Belyanin, A.; Raschke, M. B. Ultrafast Coherent Nonlinear Nanooptics and Nanoimaging of Graphene. *Nat. Nanotechnol.* **2019**, *14* (9), 838–843.
- (11) Wehmeier, L.; Lang, D.; Liu, Y.; Zhang, X.; Winnerl, S.; Eng, L. M.; Kehr, S. C. Polarization-Dependent near-Field Phonon Nanoscopy of Oxides: SrTiO₃, LiNbO₃, and PbZr_{0.2}Ti_{0.8}O₃. *Phys. Rev. B: Condens. Matter Mater. Phys.* **2019**, *100* (3), 035444.
- (12) Mittleman, D. M.; Gupta, M.; Neelamani, R.; Baraniuk, R. G.; Rudd, J. V.; Koch, M. Recent Advances in Terahertz Imaging. *Appl. Phys. B: Lasers Opt.* **1999**, *68*, 1085.
- (13) Chen, H.-T.; Kersting, R.; Cho, G. C. Terahertz Imaging with Nanometer Resolution. *Appl. Phys. Lett.* **2003**, *83* (15), 3009–3011.
- (14) Wang, K.; Mittleman, D. M.; Van Der Valk, N. C. J.; Planken, P. C. M. Antenna Effects in Terahertz Apertureless Near-Field Optical Microscopy. *Appl. Phys. Lett.* **2004**, *85* (14), 2715–2717.
- (15) Dai, G.; Geng, G.; Zhang, X.; Wang, J.; Chang, T.; Cui, H.-L. W-Band Near-Field Microscope. *IEEE Access* **2019**, *7*, 48060–48067.
- (16) Aghamiri, N. A.; Huth, F.; Huber, A. J.; Fali, A.; Hillenbrand, R.; Abate, Y. Hyperspectral Time-Domain Terahertz Nano-Imaging. *Opt. Express* **2019**, *27* (17), 24231.
- (17) Klarskov, P.; Kim, H.; Colvin, V. L.; Mittleman, D. M. Nanoscale Laser Terahertz Emission Microscopy. *ACS Photonics* **2017**, *4* (11), 2676–2680.
- (18) Alonso-González, P.; Nikitin, A. Y.; Gao, Y.; Woessner, A.; Lundeberg, M. B.; Principi, A.; Forcellini, N.; Yan, W.; Vélez, S.; Huber, A. J.; et al. Acoustic Terahertz Graphene Plasmons Revealed by Photocurrent Nanoscopy. *Nat. Nanotechnol.* **2017**, *12* (1), 31–35.
- (19) von Ribbeck, H.-G.; Brehm, M.; van der Weide, D. W.; Winnerl, S.; Drachenko, O.; Helm, M.; Keilmann, F. Spectroscopic THz Near-Field Microscope. *Opt. Express* **2008**, *16* (5), 3430–3438.
- (20) Huber, A. J.; Keilmann, F.; Wittborn, J.; Aizpurua, J.; Hillenbrand, R. Terahertz Near-Field Nanoscopy of Mobile Carriers in Single Semiconductor Nanodevices. *Nano Lett.* **2008**, *8* (11), 3766–3770.
- (21) Lin, K.-T.; Komiyama, S.; Kim, S.; Kawamura, K.; Kajihara, Y. Improved Signal-to-Noise Ratio in a Passive THz near-Field Microscope Equipped with a Helium-Free Cryostat. *2016 41st International Conference on Infrared, Millimeter, and Terahertz waves (IRMMW-THz)*; IEEE, 2016; Vol. 17, pp 1–2, DOI: 10.1109/IRMMW-THz.2016.7758551.
- (22) Kuschewski, F.; Von Ribbeck, H. G.; Döring, J.; Winnerl, S.; Eng, L. M.; Kehr, S. C. Narrow-Band near-Field Nanoscopy in the Spectral Range from 1.3 to 8.5 THz. *Appl. Phys. Lett.* **2016**, *108* (11), 113102.
- (23) Stinson, H. T.; Sternbach, A.; Najera, O.; Jing, R.; McLeod, A. S.; Slusar, T. V.; Mueller, A.; Andreev, L.; Kim, H. T.; Rozenberg, M.; et al. Imaging the Nanoscale Phase Separation in Vanadium Dioxide Thin Films at Terahertz Frequencies. *Nat. Commun.* **2018**, *9* (1), 3604.
- (24) Zhang, J.; Chen, X.; Mills, S.; Ciavatti, T.; Yao, Z.; Mescall, R.; Hu, H.; Semenenko, V.; Fei, Z.; Li, H.; et al. Terahertz Nanoimaging of Graphene. *ACS Photonics* **2018**, *5* (7), 2645–2651.
- (25) Liewald, C.; Mastel, S.; Hesler, J.; Huber, A. J.; Hillenbrand, R.; Keilmann, F. All-Electronic Terahertz Nanoscopy. *Optica* **2018**, *5* (2), 159.
- (26) Giordano, M. C.; Mastel, S.; Liewald, C.; Columbo, L. L.; Brambilla, M.; Viti, L.; Politano, A.; Zhang, K.; Li, L.; Davies, A. G.; et al. Phase-Resolved Terahertz Self-Detection near-Field Microscopy. *Opt. Express* **2018**, *26* (14), 18423.
- (27) Mastel, S.; Lundeberg, M. B.; Alonso-González, P.; Gao, Y.; Watanabe, K.; Taniguchi, T.; Hone, J.; Koppens, F. H. L.; Nikitin, A. Y.; Hillenbrand, R. Terahertz Nanofocusing with Cantilevered Terahertz-Resonant Antenna Tips. *Nano Lett.* **2017**, *17* (11), 6526–6533.
- (28) Maissen, C.; Chen, S.; Nikulina, E.; Govyadinov, A.; Hillenbrand, R. Probes for Ultra-Sensitive THz Nanoscopy. *ACS Photonics* **2019**, *6* (5), 1279–1288.
- (29) Stefanon, I.; Blaize, S.; Bruyant, A.; Aubert, S.; Lerondel, G.; Bachelot, R.; Royer, P. Heterodyne Detection of Guided Waves Using a Scattering-Type Scanning near-Field Optical Microscope. *Opt. Express* **2005**, *13* (14), 5553–5564.
- (30) Mastel, S.; Govyadinov, A. A.; Maissen, C.; Chuvilin, A.; Berger, A.; Hillenbrand, R. Understanding the Image Contrast of Material Boundaries in IR Nanoscopy Reaching 5 Nm Spatial Resolution. *ACS Photonics* **2018**, *5* (8), 3372–3378.
- (31) Moon, K.; Do, Y.; Lim, M.; Lee, G.; Kang, H.; Park, K.-S.; Han, H. Quantitative Coherent Scattering Spectra in Apertureless Terahertz Pulse Near-Field Microscopes. *Appl. Phys. Lett.* **2012**, *101* (1), 011109.
- (32) Knoll, B.; Keilmann, F.; Kramer, A.; Guckenberger, R. Contrast of Microwave Near-Field Microscopy. *Appl. Phys. Lett.* **1997**, *70* (20), 2667–2669.
- (33) Völcker, M.; Krieger, W.; Walther, H. Laser-Frequency Mixing in a Scanning Force Microscope and Its Application to Detect Local Conductivity. *J. Vac. Sci. Technol., B: Microelectron. Process. Phenom.* **1994**, *12* (3), 2129.
- (34) Völcker, M.; Krieger, W.; Walther, H. Detection of Local Conductivity by Laser-frequency Mixing in a Scanning Force Microscope. *J. Appl. Phys.* **1993**, *74* (9), 5426–5431.
- (35) Gomila, G.; Gramse, G.; Fumagalli, L. Finite-Size Effects and Analytical Modeling of Electrostatic Force Microscopy Applied to Dielectric Films. *Nanotechnology* **2014**, *25* (25), 255702.
- (36) Hu, J.; Xiao, X.; Salmeron, M. Scanning Polarization Force Microscopy: A Technique for Imaging Liquids and Weakly Adsorbed Layers. *Appl. Phys. Lett.* **1995**, *67* (4), 476–478.
- (37) Davis, L. C.; Reitz, J. R. Solution to Potential Problems near a Conducting Semi-Infinite Sheet or Conducting Disk. *Am. J. Phys.* **1971**, *39* (10), 1255–1265.
- (38) Friedberg, R. The Electrostatics and Magnetostatics of a Conducting Disk. *Am. J. Phys.* **1993**, *61* (12), 1084–1096.
- (39) Chen, X.; Lo, C. F. B.; Zheng, W.; Hu, H.; Dai, Q.; Liu, M. Rigorous Numerical Modeling of Scattering-Type Scanning near-Field Optical Microscopy and Spectroscopy. *Appl. Phys. Lett.* **2017**, *111* (22), 223110.

- (40) Esteban, R.; Vogelgesang, R.; Kern, K. Full Simulations of the Apertureless Scanning near Field Optical Microscopy Signal: Achievable Resolution and Contrast. *Opt. Express* **2009**, *17* (4), 2518.
- (41) Brehm, M.; Schliesser, A.; Cajko, F.; Tsukerman, I.; Keilmann, F. Antenna-Mediated Back-Scattering Efficiency in Infrared near-Field Microscopy. *Opt. Express* **2008**, *16* (15), 11203.
- (42) Chui, S. T.; Chen, X.; Hu, H.; Hu, D.; Dai, Q.; Liu, M. Photo-Induced Charge Density Distribution in Metal Surfaces and Its Extraction with Apertureless near-Field Optics. *J. Phys.: Condens. Matter* **2019**, *31* (24), 24LT01.
- (43) Xu, Y.; Tucker, E.; Boreman, G.; Raschke, M. B.; Lail, B. A. Optical Nanoantenna Input Impedance. *ACS Photonics* **2016**, *3* (5), 881–885.
- (44) Alonso-Gonzalez, P.; Schnell, M.; Sarriugarte, P.; Sobhani, H.; Wu, C.; Arju, N.; Khanikaev, A.; Golmar, F.; Albella, P.; Arzubiaga, L.; et al. Real-Space Mapping of Fano Interference in Plasmonic Metamolecules. *Nano Lett.* **2011**, *11* (9), 3922–3926.
- (45) Degl'Innocenti, R.; Wallis, R.; Wei, B.; Xiao, L.; Kindness, S. J.; Mitrofanov, O.; Braeuninger-Weimer, P.; Hofmann, S.; Beere, H. E.; Ritchie, D. A. Terahertz Nanoscopy of Plasmonic Resonances with a Quantum Cascade Laser. *ACS Photonics* **2017**, *4* (9), 2150–2157.
- (46) Cvitkovic, A.; Ocelic, N.; Hillenbrand, R. Analytical Model for Quantitative Prediction of Material Contrasts in Scattering-Type near-Field Optical Microscopy. *Opt. Express* **2007**, *15* (14), 8550.
- (47) McLeod, A. S.; Kelly, P.; Goldflam, M. D.; Gainsforth, Z.; Westphal, A. J.; Dominguez, G.; Thiemens, M. H.; Fogler, M. M.; Basov, D. N. Model for Quantitative Tip-Enhanced Spectroscopy and the Extraction of Nanoscale-Resolved Optical Constants. *Phys. Rev. B: Condens. Matter Mater. Phys.* **2014**, *90* (8), 085136.
- (48) Jiang, B.-Y.; Zhang, L. M.; Castro Neto, A. H.; Basov, D. N.; Fogler, M. M. Generalized Spectral Method for Near-Field Optical Microscopy. *J. Appl. Phys.* **2016**, *119* (5), 054305.
- (49) Mooshammer, F.; Sandner, F.; Huber, M. A.; Zizlsperger, M.; Weigand, H.; Plankl, M.; Weyrich, C.; Lanus, M.; Kampmeier, J.; Mussler, G.; et al. Nanoscale Near-Field Tomography of Surface States on $(\text{Bi}_{0.5}\text{Sb}_{0.5})_2\text{Te}_3$. *Nano Lett.* **2018**, *18* (12), 7515–7523.
- (50) Hauer, B.; Engelhardt, A. P.; Taubner, T. Quasi-Analytical Model for Scattering Infrared near-Field Microscopy on Layered Systems. *Opt. Express* **2012**, *20* (12), 13173.
- (51) Zhang, L. M.; Andreev, G. O.; Fei, Z.; McLeod, A. S.; Dominguez, G.; Thiemens, M.; Castro-Neto, A. H.; Basov, D. N.; Fogler, M. M. Near-Field Spectroscopy of Silicon Dioxide Thin Films. *Phys. Rev. B: Condens. Matter Mater. Phys.* **2012**, *85* (7), 075419.
- (52) Huber, A. J.; Kazantsev, D.; Keilmann, F.; Wittborn, J.; Hillenbrand, R. Simultaneous IR Material Recognition and Conductivity Mapping by Nanoscale Near-Field Microscopy. *Adv. Mater.* **2007**, *19* (17), 2209–2212.
- (53) Govyadinov, A. A.; Mastel, S.; Golmar, F.; Chuvilin, A.; Carney, P. S.; Hillenbrand, R. Recovery of Permittivity and Depth from Near-Field Data as a Step toward Infrared Nanotomography. *ACS Nano* **2014**, *8* (7), 6911–6921.
- (54) Dorfmueller, J.; Dregely, D.; Esslinger, M.; Khunsin, W.; Vogelgesang, R.; Kern, K.; Giessen, H. Near-Field Dynamics of Optical Yagi-Uda Nanoantennas. *Nano Lett.* **2011**, *11* (7), 2819–2824.
- (55) Robertson, J. Near-Field Optical Imaging of Noble Metal Nanoparticles. *Eur. Phys. J.: Appl. Phys.* **2004**, *28*, 265–291.
- (56) Schnell, M.; Garcia-Etxarri, A.; Alkorta, J.; Aizpurua, J.; Hillenbrand, R. Phase-Resolved Mapping of the Near-Field Vector and Polarization State in Nanoscale Antenna Gaps. *Nano Lett.* **2010**, *10* (9), 3524–3528.